Tuning Magnetic Droplets in Nanocontact Spin-Torque Oscillators Using Electric Fields

Cuixiu Zheng,[1] Mykola Dvornik,[2] Chengjie Wang,[1] Dun Xiao,[1] Yaowen Liu,[1,3,*] Zongzhi Zhang,[1] Yan Zhou,[4] Hamid Mazraati,[5] Martina Ahlberg,[2] Ahmad A. Awad,[2] and Johan Åkerman[2,5,†]

[1] *Shanghai Key Laboratory for Special Artificial Microstructure Materials and Technology, School of Physics, Science, and Engineering, Tongji University, Shanghai 200092, China*

[2] *Department of Physics, University of Gothenburg, 412 96 Gothenburg, Sweden*

[3] *Department of Optical Science and Engineering, Fudan University, Shanghai 200433, China*

[4] *School of Science and Engineering, The Chinese University of Hong Kong, Shenzhen 518172, China*

[5] *Materials Physics, School of Information and Communication Technology, KTH Royal Institute of Technology, Electrum 229, 164 40 Kista, Sweden*

(Received 19 February 2020; revised 19 August 2020; accepted 31 August 2020; published 2 November 2020)

Reliable *in situ* control of spin wave (SW) excitation between localized and propagating SW modes is of great interest for both fundamental and applied spintronics and magnonics. While spin-transfer-torque-generated SWs can typically be tuned directly via the driving current, the frequency of the highest intensity SWs, achieved in the strongly self-localized magnetic droplet soliton, is virtually current independent, as the droplet frequency is given by the intrinsic material properties. Here, we demonstrate, using micromagnetic simulations, how the droplet frequency can be efficiently tuned by an applied voltage through the effect of electric field (*E*-field)-dependent perpendicular magnetic anisotropy (PMA). It is found that as the PMA decreases, the droplet begins to distort and eventually collapses to give way to propagating SWs. However, due to the geometrically confined structures, the radially propagating SWs are reflected by the periphery boundary of the sample, and then the forward and backward SWs superpose to produce a series of standing SWs. The node number of the standing SWs strongly depends on the sample size as well as the applied *E* field. These findings provide a deeper understanding of magnetic excitation properties, which will be helpful for designing advanced spintronic devices.

DOI: 10.1103/PhysRevApplied.14.054001

I. INTRODUCTION

Magnetization manipulations by electric methods, including spin-transfer torque (STT) [1,2], spin-orbit torque [3,4], and electric-field (*E*-field) effects [5–7], have attracted a great deal of interest due to the rich fundamental physics for studying magnetic dynamics at nanoscale sizes as well as promising applications in spintronic devices. Magnetization precession driven by a spin polarized current can be used to design frequency-tunable spintronic devices, namely spin-torque nano-oscillators (STNOs) [8], or by a pure spin current, namely spin Hall nano-oscillators (SHNOs) [9]. Under sufficiently high currents, the magnetic damping in such nano-oscillator devices can be fully compensated by current-induced spin torques, leading to self-sustained magnetization oscillations. In order to confine the current on the nanoscale to reach the required current densities, the STNO is often accomplished by fabricating a nanocontact (NC) on top of an extended magnetic/nonmagnetic multilayer [10,11]. Typically, the STT-generated magnetodynamics is strongly nonlinear with significant current-controlled frequency tunability. If such devices are magnetized in a way that the nonlinearity of the system is positive, then high-intensity coherent propagating spin waves (SWs) can be excited [10–22] with a precession frequency higher than the SW gap of the extended film [23]. On the other hand, when the nonlinearity of the system is negative, or a confining potential is introduced (e.g., via a nonuniform Oersted field or demagnetizing field), the high-intensity self-sustained magnetization dynamics can become self-localized [21,22,24] and/or field-localized [25], respectively, with a precession frequency inside the SW gap.

A type of strongly self-localized oscillation mode—the dissipative droplet soliton—has been theoretically predicted [26,27] and experimentally reported in a STNO with a free layer having strong perpendicular magnetic anisotropy (PMA) [28,29]. In such droplet-based STNOs, the STT switches the magnetization beneath the NC, resulting in a coherent magnetization dynamics with a very large precession angle at the NC perimeter [28–34].

*yaowen@tongji.edu.cn
†johan.akerman@physics.gu.se

Interestingly, the power output of such a droplet mode in the giant magnetoresistance (GMR) sandwich structure is almost 40 times greater than that of the ferromagnetic resonance (FMR) mode [28]. If the droplet is generated in a magnetic tunnel junction, the microwave output power should be significantly enhanced, which is of great importance to reach sufficient levels for application requirement of STNOs [35]. However, as shown in both theory [26] and experiment [28], the droplet frequency is virtually independent of current, which greatly limits its usefulness for communication applications, where frequency modulation is required for efficient transfer of information. On the other hand, the SHNOs driven by pure spin currents could also induce self-excitation of coherent magnetization dynamics [9,36], in which the interaction of pure spin currents with magnetization through the spin-orbit torque is used to amplify or suppress the magnetization oscillations [37,38]. Such type of oscillators would have advantages over conventional STNOs due to the rather simple fabrication process and relatively low driving current [39–41].

It is well known that the tunable magnetization dynamics (switching and precession) can be manipulated by using E fields through the voltage-controlled magnetic anisotropy (VCMA) effect in the Co-Fe-B/MgO system [42–44], which extends opportunities for manipulation of magnetization dynamics in spintronic devices. This versatile technique can result in significant reductions in power consumption [45]. In this paper, the VCMA effect is introduced into magnetic-droplet-based STNOs. We show that the E field can directly tune the microwave frequency of the magnetic droplet oscillator. As the PMA decreases with the applied E field, the droplet begins to distort and eventually collapses to give way to propagating SWs.

II. MODEL AND SIMULATIONS

Figure 1(a) shows a schematic of the E-field-tunable STNO structure. It consists of a magnetic tunnel junction [46,47] or GMR pillar [28] with a NC on top of the fixed spin polarizing layer (reference layer, e.g., a Co/Pt multilayer; see Supplemental Material A for details). The free layer has PMA and can be made of a [Co/Ni] multilayer [28,48] or a $Co_{40}Fe_{40}B_{20}$ layer [49]. Besides, an additional oxide layer (e.g., MgO with thickness $t > 1.0$ nm) is introduced below the free layer as a dielectric capacitor. We suppose that applying a voltage across this oxide layer can induce accumulation of electric charges at the interface connected to the free layer, as illustrated in Fig. 1(a), leading to an E field acting on the free layer and changing its PMA via the VCMA effect [50]. Specifically, a negative

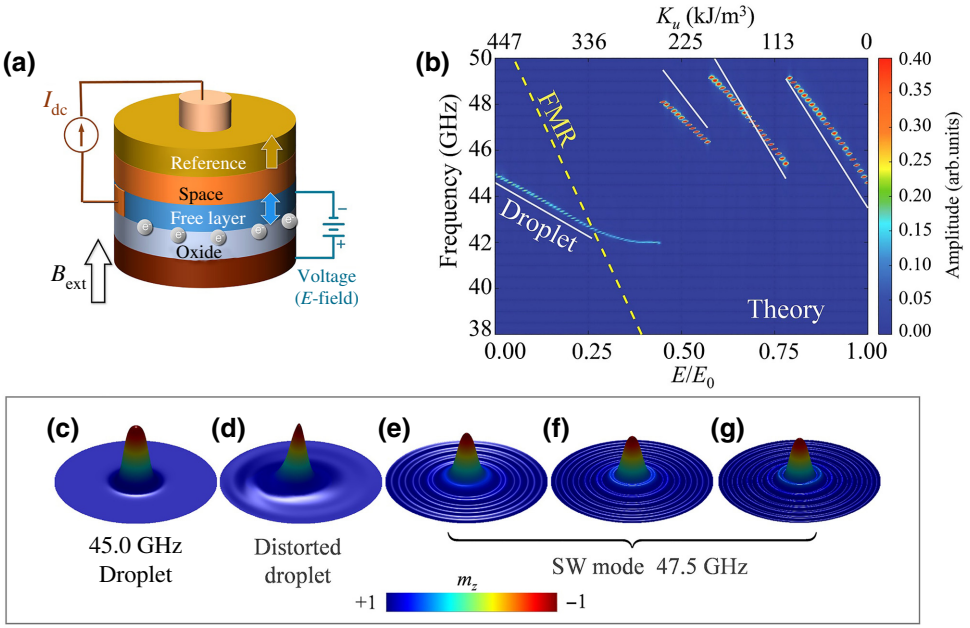

FIG. 1. Electric field control of STT-driven magnetization oscillations in a NC STNO. (a) Schematic of a NC STNO under the co-action of electric field and spin-polarized current. The perpendicular polarizing reference layer could consist of Co/Pt, and the free layer is made of [Co/Ni]/Co-Fe-B films. The oxide layer below the free layer serves as a dielectric capacitor and generates an electric field. The magnetic field is applied along the $+z$ direction. Positive current is applied from the polarizer layer to the free layer. (b) Frequency characteristics of the excited modes as a function of electric field (bottom x axis) and PMA (top x axis). The dashed yellow line represents the calculated uniform FMR frequency using Eq. (5). The solid white lines show the analytical calculation results of the same quantities using Eqs. (4) and (6), respectively. Three types of modes are identified by the topography of m_z: (c) magnetic droplet mode, (d) distorted droplet mode, and (e)–(g) spin wave modes with different periodic numbers n (related to the wave number): $n = 5$, 6, and 7, respectively. For clarity, the topographies of m_z in (c)–(g) are turned upside down.

voltage decreases the effective PMA ($K_{\rm eff}$) of the free layer as [51]

$$K_{\rm eff} = K_0 - \xi \frac{E}{d} \tag{1}$$

where the electric field $E = V/t$ [42,52], V is the applied voltage, and t is the thickness of dielectric oxide layer. d (=1 nm) is the free layer thickness. K_0 is the perpendicular anisotropy at $V = 0$. ξ is the VCMA (magnetoelectric) coefficient used to parameterize the dependence of the PMA on the applied electric field. The typical values of ξ are in the range of 30–50 fJ/V m [53]. In this study, we choose $\xi = 50$ fJ/V m and $K_0 = 447$ kJ/m^3 [30]. According to Eq. (1), the effective anisotropy $K_{\rm eff}$ can be reduced to zero if an electric field of $E_0 = 8.9$ V/nm is applied. We suppose both the STNO and NC have circular shapes with corresponding radii of $R = 256$ nm and $R_{\rm NC} = 30$ nm, respectively, unless specified.

The simulations are performed using the open-source simulation software MUMAX3 [54], which is based on the Landau-Lifshitz-Gilbert-Slonczewski equation:

$$\frac{d\mathbf{m}}{dt} = -\gamma \mathbf{m} \times \mathbf{H}_{\rm eff} + \alpha \mathbf{m} \times \frac{d\mathbf{m}}{dt} + a_J \mathbf{m} \times (\mathbf{m} \times \mathbf{m_p}), \tag{2}$$

where $\mathbf{m} = \mathbf{M}/M_s$ is the unit magnetization vector of the free layer, M_s is the free layer saturation magnetization, α is the Gilbert damping factor, and γ is the gyromagnetic ratio. $\mathbf{H}_{\rm eff}$ is the effective magnetic field that includes exchange, anisotropy, demagnetizing (H_d), and external magnetic fields ($H_{\rm ext}$). For simplicity, the current-induced Oersted field [17,55,56] is ignored in this study. The effective magnetic field reads

$$\mathbf{H}_{\rm eff} = \frac{2A_{\rm ex}}{\mu_0 M_s} \nabla^2 \mathbf{m} + \frac{2K_{\rm eff}}{\mu_0 M_s} m_z \hat{\mathbf{z}} + \mathbf{H}_d + H_{\rm ext} \hat{\mathbf{z}}, \tag{3}$$

where $A_{\rm ex}$ is the exchange stiffness and μ_0 is the vacuum permeability. The last term of Eq. (2) describes the STT effect. The torque factor $a_J = \hbar \gamma P J/(2|e|M_s d)$, which depends on the current density J, the thickness of the free layer d, and the spin polarization P. In this study, the typical material parameters are taken for the free layer as follows [30]: the saturation magnetization $M_s = 716$ kA/m, exchange stiffness $A_{\rm ex} = 30$ pJ/m, Gilbert damping $\alpha = 0.05$, and $P = 0.5$. A discretization cell of $2 \times 2 \times 1$ nm^3 is used.

III. RESULTS AND DISCUSSION

A. Droplet mode and its frequency

Figure 1(b) shows the frequency response of the NC STNO as a function of E field. Here the applied current is $I = 4.0$ mA and perpendicular magnetic field $\mu_0 H_{\rm ext} = 1.5$ T. The frequency is calculated using the fast Fourier transform technique on the time traces of the in-plane component of magnetization averaged over the NC area [57]. Basically, three parameter regimes with distinct types of magnetization dynamics can be identified. First, a magnetic droplet state [Fig. 1(c)] is sustained with a frequency well below the FMR frequency for low E fields. As the E field increases, the droplet frequency crosses the FMR curve at $E = 0.28E_0 = 2.49$ V/nm ($K_{\rm eff} = 322$ kJ/m^3). After that, a distorted droplet is observed [see Fig. 1(d)]. Finally, when the E field is increased over a certain threshold $E = 0.45E_0$ (i.e., $K_{\rm eff} = 247$ kJ/m^3), the magnetization dynamics is pushed completely above the FMR, which drives the system into propagating SW excitation modes [Figs. 1(e)–1(g)].

Figure 1(c) shows a typical topography of a magnetic droplet, which is characterized by the z-component of the magnetization (m_z). For clarity, these topographies of m_z are turned upside down. Note that the spins located outside of the NC are along the $+z$ direction due to the strong PMA and the perpendicular magnetic field. The spins underneath the NC are reversed to the $-z$ direction by the STT action. The self-oscillation occurs due to the energy balance between the energy supply into the free layer by the STT and the energy dissipation of the damping. Movie 1 within the Supplemental Material shows the magnetization oscillation dynamics of the droplet mode, in which the spins on the NC perimeter rotate coherently in-plane along the counterclockwise direction [58].

As shown in Fig. 1(b), the simulated oscillation frequency of the magnetic droplet decreases with decreasing anisotropy $K_{\rm eff}$ (i.e., increasing E field). Theoretically, the droplet frequency reads (see Supplemental Material B for details) [26,59,60]:

$$\omega_{\rm MD} = \gamma_0 \mu_0 \left[H + \left(\frac{2K_{\rm eff}}{\mu_0 M_s} - M_s \right) \frac{\omega_p}{\omega_{\rm FMR}} \right], \tag{4}$$

where the gyromagnetic ratio $\gamma_0 = 28$ GHz/T, ω_p is the precession frequency of the magnetization in the absence of an external magnetic field, and $\omega_{\rm FMR}$ is the uniform FMR frequency of the system:

$$\omega_{\rm FMR} = \gamma_0 \mu_0 \left[H + \left(\frac{2K_{\rm eff}}{\mu_0 M_s} - M_s \right) \right]. \tag{5}$$

Note that the simulated frequency of the droplet mode (blue curve) in Fig. 1(b) agrees well with the theoretical prediction (white curve) using Eq. (4). Moreover, the typical feature that the droplet frequency is lower than the uniform FMR frequency also supports previous theoretical [26] and experimental studies [28].

B. Distorted droplet mode

The magnetic droplet state remains until the E field is greater than $0.28E_0$ ($K_{\rm eff} = 322$ kJ/m^3), where the PMA

energy starts to be lower than the demagnetization energy (not shown), and the balance between the effective field and the STT is also destroyed. Moreover, calculations of the disk's eigenmodes show that the density of SW states is very high in the vicinity of the FMR [see Fig. S2(c) within the Supplemental Material]. This result implies that the droplet at these parameters scatters with the SWs propagating along a certain direction. Consequently, the magnetization topography of the droplet is distorted to be an asymmetric excitation mode, namely a distorted magnetic droplet oscillation mode [Fig. 1(d)].

C. Propagating spin wave mode

When the electric field is further increased to $E > 0.45E_0$ ($K_{\rm eff} < 247$ kJ/m^3), a series of radial propagating spin waves, i.e., the so-called Slonczewski mode, are generated [15,26,47]. For a geometrically confined structure, these radial propagating SWs will be reflected by the periphery boundary of the sample. In this case, depending on the strength of the E field, the forward and backward SWs will superpose to produce a series of standing SWs, as shown in Figs. 1(e)–1(g), in which the magnetization topographies of these modes are given. A typical movie (movie-2.mp4) of the standing SW mode is shown in the Supplemental Material [58].

Theoretically, the dispersion relation for the SW modes satisfies the following formula (see Supplemental Material C for details) [26,61]:

$$\omega_{\rm SW} = \omega_{\rm FMR} + \frac{2\gamma_0 A_{\rm ex}}{M_s}k^2, \tag{6}$$

where $A_{\rm ex}$ is the exchange constant of the material and $k = 2\pi/\lambda$ is the wave number of the excited SWs (λ is the wavelength), by which the existence of the periodic node or antinode number (integer n) of SWs in the confined structure can be determined:

$$n = (R - R_{\rm NC})k/2\pi. \tag{7}$$

By taking $\omega_{\rm SW} = 47.5$ GHz, $R = 256$ nm, $R_{\rm NC} = 30$ nm, and $K = (0\text{–}0.55)K_0$ in Eqs. (5)–(7), one can analytically obtain the node number n that is allowed to exist in the confined sample: $n = 5$, 6, and 7 for different $K_{\rm eff}$. These theoretically predicted values perfectly agree with our simulations as shown in Figs. 1(b) and 1(e)–1(g).

More intuitively, in Fig. 2(e) we have plotted the overlaid snapshots from the time evolution of the standing SW profiles for $n = 6$ (at $R = 250$ nm), in which six antinodes are clearly observed. Consistent with the analytical theory, the observed standing SW modes with $n = 5$, 6, and 7 in Fig. 1(b) show three clear branches of frequency curves as the anisotropy is tuned by the E field. For each SW mode with a given n, the frequency decreases with the E field, which can be well described by the theoretical expression in Eq. (6) and the reduction of $K_{\rm eff}$ by the E field. The frequencies of these standing SWs vary between 40 and 50 GHz and are higher than the uniform FMR frequency.

Depending on the sample size of confined structures, the allowed periodic number of standing SW modes continuously increases for large samples. Figures 2(d) and 2(e) show the allowed standing SW modes as R varies from 250

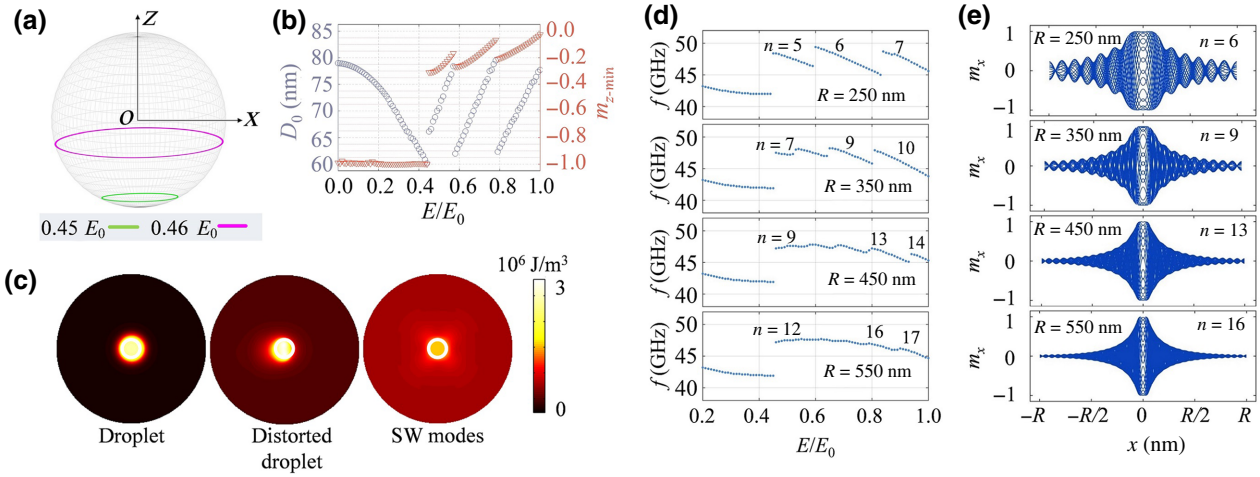

FIG. 2. Spin wave modes. (a) Stable precession trajectories of magnetization at $E = 0.45E_0$ (i.e., $K_{\rm eff} = 247$ kJ/m^3) and $0.46E_0$ ($K_{\rm eff} = 242$ kJ/m^3). (b) Dependence of the droplet magnetization profile diameter (D_0) and the minimum value of the z component of magnetization at the center of NC ($m_{z-\rm min}$) as a function of applied E field. (c) Total energy density of the three modes excited at $I = 4.0$ mA and $\mu_0 H_{\rm ext} = 1.5$ T. The scale of the color bar is normalized to the highest density reaching a value of 3×10^6 J/m^3. The white solid circles denote the NC region. (d) The numerically simulated frequency characteristics of the excited modes for different sizes of nanopillars, where the NC is fixed at $R_{\rm NC} = 30$ nm. (e) Overlaid snapshots for the time evolution of the standing spin wave profiles for samples with different sizes and different periodic numbers n.

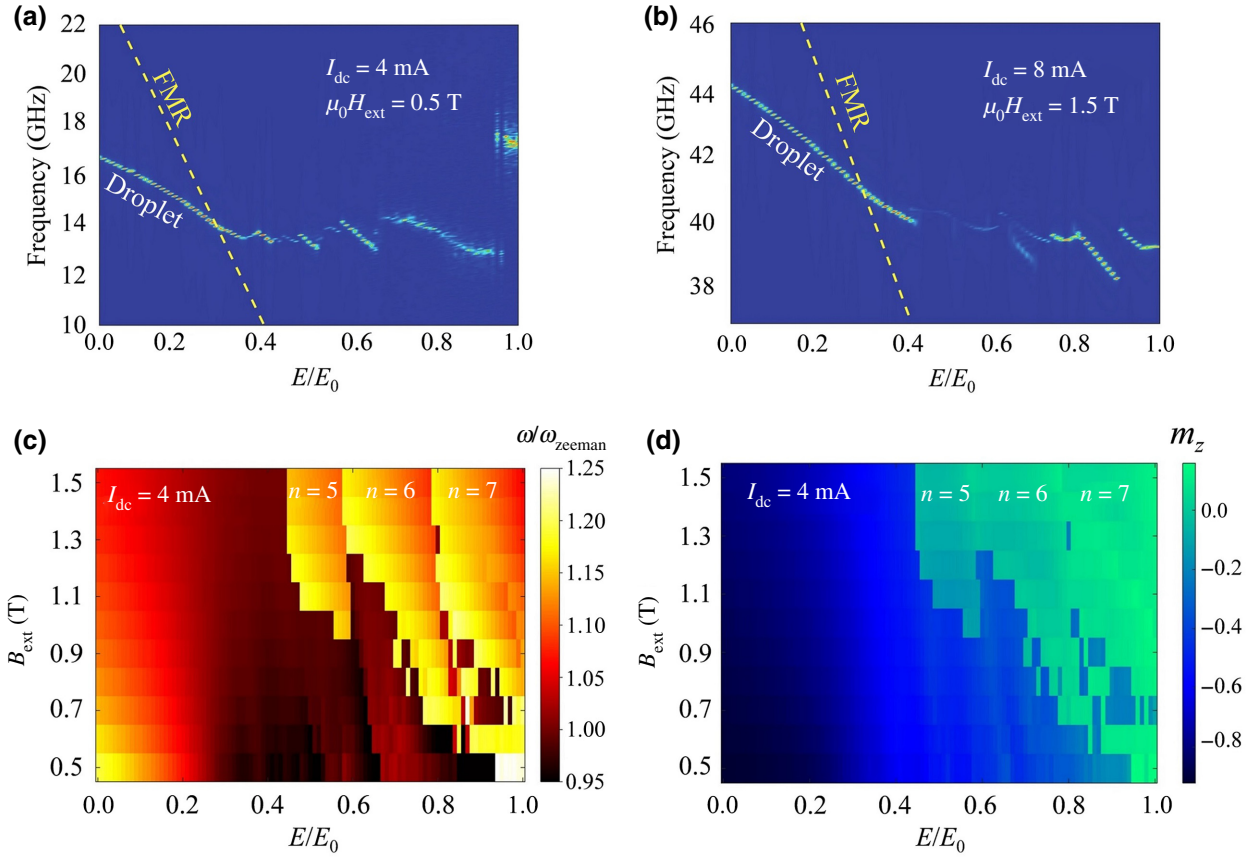

FIG. 3. Excited mode frequency dependence on applied E field for devices with $R = 256$ nm and $R_{NC} = 30$ nm. (a) A smaller magnetic field compared with Fig. 1(b) ($I = 4$ mA and $B_{ext} = 0.5$ T). (b) A larger applied current compared with Fig. 1(b) ($I = 8$ mA and $B_{ext} = 1.5$ T). (c) The frequency (ω/ω_{Zeeman}) and (d) the z-component of the magnetization within the NC region as a function of magnetic field and E field, respectively, where $I = 4$ mA and $\omega_{Zeeman} = \gamma H_{ext}$. A smaller magnetic field reduces the frequency of the SW mode and the magnetization underneath the NC tends to the $-z$ direction.

to 550 nm and some typical overlaid profiles of these standing SW modes, in which the antinode numbers are clearly identified for each size of sample. As the sample size increases (e.g., $R > 550$ nm), the frequency jump between different standing SW modes will be less abrupt, which implies that the standing SW mode will transform into the continuously propagating SW mode for large or unconfined samples (see D and Fig. S4 within the Supplemental Material).

To further gain insight into the different excitation modes, we calculate the spatial distributions of the magnetic energy density $\mathscr{E}$ in Fig. 2(c). Note that the energy density of the droplet mode is almost localized into the area underneath the NC. In contrast, the distorted droplet has a slightly asymmetric energy distribution, similar to its asymmetric magnetization configuration. For the SW modes, the energy distribution is spread over the whole disk via the propagating SWs.

It is worth noting that the E field not only allows one to change the mode character (e.g., wave number) and frequency, but also to tune the size of the reversed magnetization region. This is attributed to the change of the effective field due to the reduction of the PMA by the E field. Figure 2(b) shows the effective diameter D_0 and depth $m_{z-\min}$ of the reversed region, where D_0 is defined as the full width at half maximum and $m_{z-\min}$ is the lowest value of the central droplet profile. In the case of the droplet mode, the spin at the NC center is almost fully reversed to the $-z$ direction, showing $D_0 = 40$ nm and $m_{z-\min} = -0.97$ at $E = 0$. When the E field increases ($0 < E \leq 0.45E_0$), $m_{z-\min}$ almost remains unchanged but D_0 decreases. This decreased droplet size gives rise to the decrease of the droplet frequency. Figure 2(a) shows two final stable precession orbits of the magnetization underneath the NC in the critical zone of transition from droplet mode to SW mode at $E = 0.45E_0$ for the distorted droplet mode (green curve) and $E = 0.46E_0$ for the SW mode (magenta curve). Note that both D_0 and $m_{z-\min}$ increase with the E field for the given SW mode.

It should be mentioned that the transition of the localized droplet mode into propagating SW modes can also be tuned by changing the direction of oblique magnetic fields

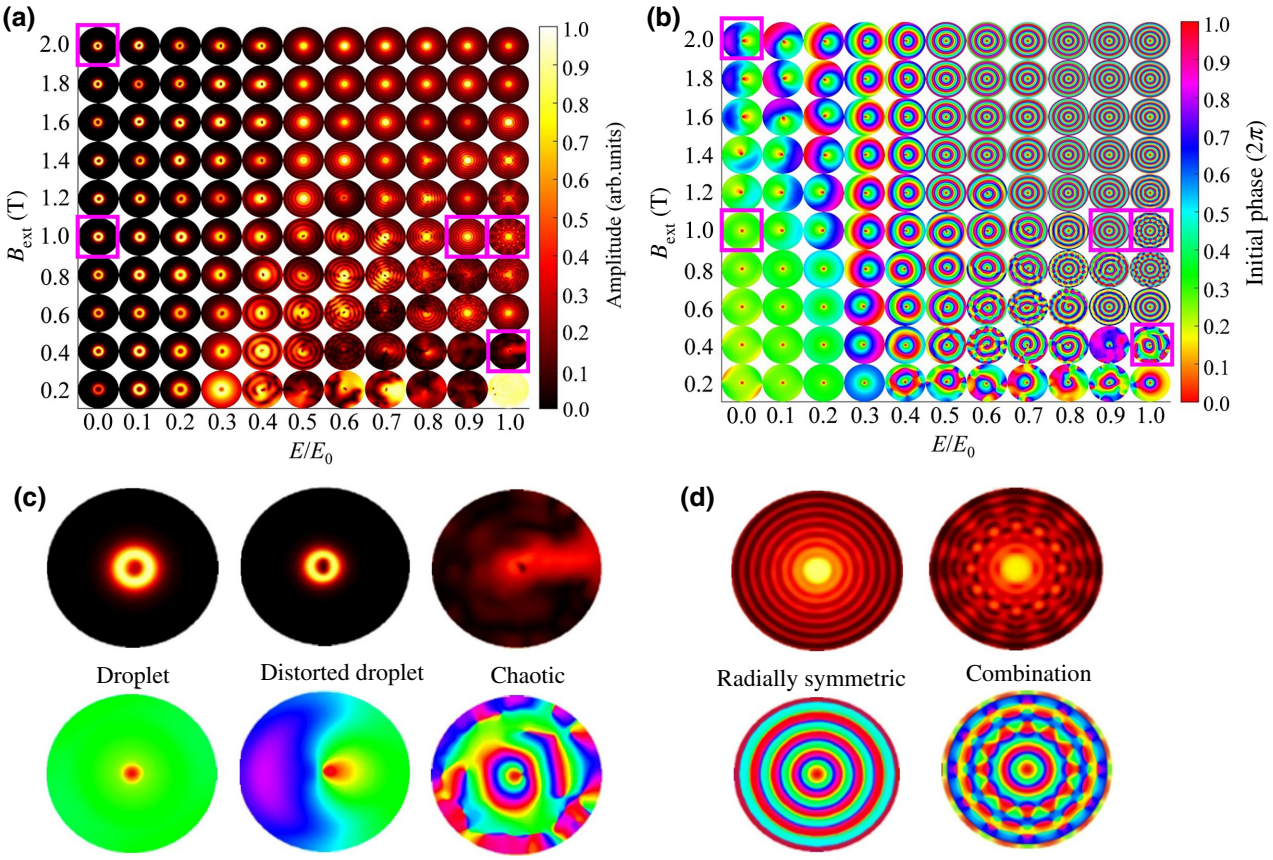

FIG. 4. Phase diagram of different oscillation eigenmodes as a function of the magnetic field and E field for a STNO with $R = 128$ nm and $R_{NC} = 30$ nm. (a) The spatial variation of the Fourier amplitude of the oscillation modes. (b) The Fourier phase variation for each state. The axially symmetric radial-like modes include both the droplet mode and SW modes at high B_{ext}. The combined radially and azimuthally symmetric modes appear at intermediate B_{ext} of 0.6–1.0 T. The excited modes become very chaotic at low B_{ext} of 0.2–0.5 T with increasing E field. (c),(d) Enlarged images of the Fourier amplitude (upper panel) and phase (lower panel) for several typical oscillation modes marked by pink squares.

[62]. In that case, it is found that the droplets nucleate in nearly perpendicular fields and that the propagating SWs tend to be the dominant mode when the external magnetic field has strong enough in-plane components.

D. Magnetic field dependence

In addition to the E field, the perpendicular magnetic field can also slightly change the dynamics of the STNO. Figures 3(a) and 3(b) show the frequency characteristics in the cases of a small magnetic field ($I = 4$ mA and $B_{ext} = 0.5$ T) and a large current ($I = 8$ mA and $B_{ext} = 1.5$ T), respectively, compared with the case shown in Fig. 1(b) with $I = 4$ mA and $B_{ext} = 1.5$ T. In Fig. 3(a), the applied magnetic field is not strong enough to dominate over the STT effect, which leads to a reduction of the droplet frequency. The propagating SW modes are also strongly suppressed. Their frequencies in Fig. 3(a) are lower than those obtained at a high magnetic field of $B_{ext} = 1.5$ T [Fig. 1(b)]. We attribute this result to the fact that all the frequencies of the excited modes (both the droplet and the SWs), as described in Eqs. (4)–(6), strongly depend on the applied perpendicular magnetic field B_{ext}. More systematic results for the field-dependent frequency diagram are summarized in Fig. 3(c), in which the magnetic field is varied from 0.5 to 1.5 T and the parameter regions for the typical three propagating SW modes of $n = 5$, 6, and 7 appear at high magnetic fields [the upper-right regions in Fig. 3(c) and 3(d)]. In this plot, the color contrast indicates the relative frequency ω/ω_{Zeeman}, where ω_{Zeeman} is the Zeeman frequency excited by the external field only [26].

To further clarify the influence of the magnetic field, we have extracted phase-sensitive Fourier transform images for various excitation modes, characterized by the Fourier amplitude and phase given in Figs. 4(a) and 4(b), respectively. In these simulations, the sample size is $R = 128$ nm. The magnetic field is varied from 0.2 to 2.0 T. For this sample, the droplet mode is stable in the parameter region of low magnetic fields and low E fields. When the magnetic

field increases, the droplet is distorted for $B_{ext} > 1.4$ T and $E/E_0 < 0.4$ [see upper-left region in Fig. 4(b)]. In this region, the observed in-plane droplet precession at the NC has lost the coherent phase, but the intrinsic physical mechanism for this phenomenon is still unclear. Axially symmetric standing SW modes with periodic numbers of $n = 5$, 6, and 7 are clearly seen in the phase [upper-right region in Fig. 4(b)]. When the magnetic field decreases, the radially symmetric SW modes lose their stability and gradually become the combined radially and azimuthally symmetric phase modes [see Fig. 4(d)]. At very low field $B_{ext} = 0.2$–0.5 T, the radially symmetric standing SW modes are further destroyed, leading to anomalous chaotic oscillation states in both amplitude and phase.

IV. CONCLUSION

In conclusion, we have demonstrated a droplet-based NC STNO structure that can be tuned with an external electric field and magnetic field. Several different types of magnetization excitation dynamics—including a droplet mode, a distorted droplet mode, standing SW modes, and even chaotic modes—can be sustained by changing the strength of the E field. The simulated frequencies are in a good qualitative agreement with theory. We expect that the proposed E-field-tunable STNOs could open up possibilities for manipulating the localized droplet excitation and controlling its transition into propagating SW modes.

ACKNOWLEDGMENTS

Y.L. acknowledges support by the National Key Research and Development Project of China (2018YFB04 07603) and the NSFC (No. 11774260 and No. 51971161). Z.Z. acknowledges the support by the NSFC (No. 51671057 and No. 11474067). Y.Z. acknowledges the support by the President's Fund of CUHKSZ, Longgang Key Laboratory of Applied Spintronics, National Natural Science Foundation of China (Grants No. 11974298 and No. 61961136006) and Shenzhen Peacock Group Program (Grant No. KQTD20180413181702403).

[1] J. C. Slonczewski, Current-driven excitation of magnetic multilayers, J. Magn. Magn. Mater. **159**, L1 (1996).
[2] L. Berger, Emission of spin waves by a magnetic multilayer traversed by a current, Phys. Rev. B **54**, 9353 (1996).
[3] A. Brataas and K. M. D. Hals, Spin-orbit torques in action, Nat. Nanotech. **9**, 86 (2014).
[4] J. Sinova, S. O. Valenzuela, J. Wunderlich, C. H. Back, T. Jungwirth, and Spin Hall effects. Rev. Mod. Phys. **87**, 1213 (2015).
[5] D. Chiba, M. Sawicki, Y. Nishitani, Y. Nakatani, F. Matsukura, and H. Ohno, Magnetization vector manipulation by electric fields, Nature **455**, 515 (2008).
[6] H. Ohno, D. Chiba, F. Matsukura, T. Omiya, E. Abe, T. Dietl, Y. Ohno, and K. Ohtani, Electric-field control of ferromagnetism, Nature **408**, 944 (2000).
[7] C.-G. Duan, J. P. Velev, R. F. Sabirianov, Z. Zhu, J. Chu, S. S. Jaswal, and E. Y. Tsymbal, Surface Magnetoelectric Effect in Ferromagnetic Metal Films, Phys. Rev. Lett. **101**, 137201 (2008).
[8] T. Chen, R. K. Dumas, A. Eklund, P. K. Muduli, A. Houshang, A. A. Awad, P. Dürrenfeld, B. G. Malm, A. Rusu, and J. Åkerman, Spin-Torque and spin-hall nano-oscillators, Proc. IEEE **104**, 1919 (2016).
[9] V. E. Demidov, S. Urazhdin, H. Ulrichs, V. Tiberkevich, A. Slavin, D. Baither, G. Schmitz, and S. O. Demokritov, Magnetic nano-oscillator driven by pure spin current, Nat. Mater. **11**, 1028 (2012).
[10] W. H. Rippard, M. R. Pufall, S. Kaka, S. E. Russek, and T. J. Silva, Direct-Current Induced Dynamics in $Co_{90}Fe_{10}/Ni_{80}Fe_{20}$ Point Contacts, Phys. Rev. Lett. **92**, 027201 (2004).
[11] F. B. Mancoff, N. D. Rizzo, B. N. Engel, and S. Tehrani, Phase-locking in double-point-contact spin-transfer devices, Nature **437**, 393 (2005).
[12] S. Kaka, M. R. Pufall, W. H. Rippard, T. J. Silva, S. E. Russek, and J. A. Katine, Mutual phase-locking of microwave spin torque nano-oscillators, Nature **437**, 389 (2005).
[13] T. J. Silva and W. H. Rippard, Developments in nano-oscillators based upon spin-transfer point-contact devices, J. Magn. Magn. Mater. **320**, 1260 (2008).
[14] W. H. Rippard, M. R. Pufall, S. Kaka, T. J. Silva, and S. E. Russek, Current-driven microwave dynamics in magnetic point contacts as a function of applied field angle, Phys. Rev. B **70**, 100406 (2004).
[15] J. C. Slonczewski, Excitation of spin waves by an electric current, J. Magn. Magn. Mater. **195**, L261 (1999).
[16] BonettiS MadamiM, TacchiS ConsoloG, GubbiottiG CarlottiG, F. B. Mancoff, M. A. Yar, and J. Akerman, Direct observation of a propagating spin wave induced by spin-transfer torque, Nat. Nanotech. **6**, 635 (2011).
[17] R. K. Dumas, E. Iacocca, S. Bonetti, S. R. Sani, S. M. Mohseni, A. Eklund, J. Persson, O. Heinonen, and J. Åkerman, Spin-Wave-Mode Coexistence on the Nanoscale: A Consequence of the Oersted-Field-Induced Asymmetric Energy Landscape, Phys. Rev. Lett. **110**, 257202 (2013).
[18] S. Sani, J. Persson, S. M. Mohseni, Y. Pogoryelov, P. K. Muduli, A. Eklund, G. Malm, M. Käll, A. Dmitriev, and J. Åkerman, Mutually synchronized bottom-up multi-nanocontact spin–torque oscillators, Nat. Commun. **4**, 2731 (2013).
[19] M. Madami, E. Iacocca, S. Sani, G. Gubbiotti, S. Tacchi, R. K. Dumas, J. Åkerman, and G. Carlotti, Propagating spin waves excited by spin-transfer torque: A combined electrical and optical study, Phys. Rev. B **92**, 024403 (2015).
[20] A. Houshang, E. Iacocca, P. Durrenfeld, S. R. Sani, J. Akerman, and R. K. Dumas, Spin-wave-beam driven synchronization of nanocontact spin-torque oscillators, Nat. Nanotech. **11**, 280 (2016).
[21] S. Bonetti, V. Tiberkevich, G. Consolo, G. Finocchio, P. Muduli, F. Mancoff, A. Slavin, and J. Åkerman, Experimental Evidence of Self-Localized and Propagating

Spin Wave Modes in Obliquely Magnetized Current-Driven Nanocontacts, Phys. Rev. Lett. **105**, 217204 (2010).

[22] S. Bonetti, V. Puliafito, G. Consolo, V. S. Tiberkevich, A. N. Slavin, and J. Åkerman, Power and linewidth of propagating and localized modes in nanocontact spin-torque oscillators, Phys. Rev. B **85**, 174427 (2012).

[23] C. Kittel, Theory of the structure of ferromagnetic domains in films and small particles, Phys. Rev. **70**, 965 (1946).

[24] A. Slavin and V. Tiberkevich, Spin Wave Mode Excited by Spin-Polarized Current in a Magnetic Nanocontact is a Standing Self-Localized Wave Bullet, Phys. Rev. Lett. **95**, 237201 (2005).

[25] R. K. Dumas, S. R. Sani, S. M. Mohseni, E. Iacocca, Y. Pogoryelov, P. K. Muduli, S. Chung, X. Du, P. Dürrenfeld, and J. Åkerman, Recent advances in nanocontact spin-torque oscillators, IEEE. Trans. Magn. **50**, 4100107 (2014).

[26] M. A. Hoefer, T. J. Silva, and M. W. Keller, Theory for a dissipative droplet soliton excited by a spin torque nanocontact, Phys. Rev. B **82**, 054432 (2010).

[27] M. A. Hoefer, M. Sommacal, and T. J. Silva, Propagation and control of nanoscale magnetic-droplet solitons, Phys. Rev. B **85**, 214433 (2012).

[28] S. M. Mohseni, S. R. Sani, J. Persson, T. N. A. Nguyen, S. Chung, Y. Pogoryelov, P. K. Muduli, E. Iacocca, A. Eklund, R. K. Dumas, S. Bonetti, A. Deac, M. A. Hoefer, and J. Åkerman, Spin torque–generated magnetic droplet solitons, Science **339**, 1295 (2013).

[29] F. Macià, D. Backes, and A. D. Kent, Stable magnetic droplet solitons in spin-transfer nanocontacts, Nat. Nanotech. **9**, 992 (2014).

[30] E. Iacocca, R. K. Dumas, L. Bookman, M. Mohseni, S. Chung, M. A. Hoefer, and J. Åkerman, Confined Dissipative Droplet Solitons in Spin-Valve Nanowires with Perpendicular Magnetic Anisotropy, Phys. Rev. Lett. **112**, 047201 (2014).

[31] S. Chung, S. M. Mohseni, S. R. Sani, E. Iacocca, R. K. Dumas, T. N. Anh Nguyen, Y. Pogoryelov, P. K. Muduli, A. Eklund, M. Hoefer, and J. Åkerman, Spin transfer torque generated magnetic droplet solitons (invited), J. Appl. Phys. **115**, 172612 (2014).

[32] S. M. Mohseni, S. R. Sani, R. K. Dumas, J. Persson, T. N. Anh Nguyen, S. Chung, Y. Pogoryelov, P. K. Muduli, E. Iacocca, A. Eklund, and J. Åkerman, Magnetic droplet solitons in orthogonal nano-contact spin torque oscillators, Phys. B: Condens. Matter **435**, 84 (2014).

[33] S. Chung, S. Majid Mohseni, A. Eklund, P. Dürrenfeld, M. Ranjbar, S. R. Sani, T. N. Anh Nguyen, R. K. Dumas, and J. Åkerman, Magnetic droplet solitons in orthogonal spin valves, Low Temp. Phys. **41**, 833 (2015).

[34] S. Chung, A. Eklund, E. Iacocca, S. M. Mohseni, S. R. Sani, L. Bookman, M. A. Hoefer, R. K. Dumas, and J. Akerman, Magnetic droplet nucleation boundary in orthogonal spin-torque nano-oscillators, Nat. Commun. **7**, 11209 (2016).

[35] A. V. Sadovnikov, E. N. Beginin, S. E. Sheshukova, Y. P. Sharaevskii, A. I. Stognij, N. N. Novitski, V. K. Sakharov, Y. V. Khivintsev, and S. A. Nikitov, Route toward semiconductor magnonics: Light-induced spin-wave nonreciprocity in a YIG/GaAs structure, Phys. Rev. B **99**, 054424 (2019).

[36] L. Chen, S. Urazhdin, K. Zhou, Y. W. Du, and R. H. Liu, Magnetic Droplet Mode in a Vertical Nanocontact-Based Spin Hall Nano-Oscillator at Oblique Fields, Phys. Rev. Appl. **13**, 024034 (2020).

[37] L. Liu, C.-F. Pai, D. C. Ralph, and R. A. Buhrman, Magnetic Oscillations Driven by the Spin Hall Effect in 3-Terminal Magnetic Tunnel Junction Devices, Phys. Rev. Lett. **109**, 186602 (2012).

[38] V. E. Demidov, S. Urazhdin, E. R. J. Edwards, M. D. Stiles, R. D. McMichael, and S. O. Demokritov, Control of Magnetic Fluctuations by Spin Current, Phys. Rev. Lett. **107**, 107204 (2011).

[39] H. Mazraati, S. R. Etesami, S. A. H. Banuazizi, S. Chung, A. Houshang, A. A. Awad, M. Dvornik, and J. Åkerman, Auto-oscillating Spin-Wave Modes of Constriction-Based Spin Hall Nano-Oscillators in Weak In-Plane Fields, Phys. Rev. Appl. **10**, 054017 (2018).

[40] A. Giordano, M. Carpentieri, A. Laudani, G. Gubbiotti, B. Azzerboni, and G. Finocchio, Spin-Hall nano-oscillator: A micromagnetic study, Appl. Phys. Lett. **105**, 042412 (2014).

[41] M. Ranjbar, P. Drrenfeld, M. Haidar, E. Iacocca, M. Balinskiy, T. Q. Le, M. Fazlali, A. Houshang, A. A. Awad, R. K. Dumas, and J. kerman, Co-Fe-B-Based spin hall nano-oscillators, IEEE Mag. Lett. **5**, 1 (2014).

[42] W.-G. Wang, M. Li, S. Hageman, and C. L. Chien, Electric-field-assisted switching in magnetic tunnel junctions, Nat. Mater. **11**, 64 (2012).

[43] Y. Shiota, T. Nozaki, F. Bonell, S. Murakami, T. Shinjo, and Y. Suzuki, Induction of coherent magnetization switching in a few atomic layers of FeCo using voltage pulses, Nat. Mater. **11**, 39 (2012).

[44] W. Zhu, D. Xiao, Y. Liu, S. J. Gong, and C.-G. Duan, Picosecond electric field pulse induced coherent magnetic switching in MgO/FePt/Pt(001)-based tunnel junctions: A multiscale study, Sci. Rep. **4**, 4117 (2014).

[45] X. Zhang, C. Wang, Y. Liu, Z. Zhang, Q. Y. Jin, and C.-G. Duan, Magnetization switching by combining electric field and spin-transfer torque effects in a perpendicular magnetic tunnel junction, Sci. Rep **6**, 18719 (2016).

[46] S. Jiang, M. Ahlberg, S. Chung, A. Houshang, R. Ferreira, P. P. Freitas, and J. Åkerman, Magnetodynamics in orthogonal nanocontact spin-torque nano-oscillators based on magnetic tunnel junctions, Appl. Phys. Lett. **115**, 152402 (2019).

[47] A. Houshang, R. Khymyn, H. Fulara, A. Gangwar, M. Haidar, S. R. Etesami, R. Ferreira, P. P. Freitas, M. Dvornik, R. K. Dumas, and J. Åkerman, Spin transfer torque driven higher-order propagating spin waves in nano-contact magnetic tunnel junctions, Nat. Commun. **9**, 4374 (2018).

[48] E. Liu, J. Swerts, S. Couet, S. Mertens, Y. Tomczak, T. Lin, V. Spampinato, A. Franquet, S. Van Elshocht, G. Kar, A. Furnemont, and J. De Boeck, [Co/Ni]-CoFeB hybrid free layer stack materials for high density magnetic random access memory applications, Appl. Phys. Lett. **108**, 132405 (2016).

[49] M. Endo, S. Kanai, S. Ikeda, F. Matsukura, and H. Ohno, Electric-field effects on thickness dependent magnetic anisotropy of sputtered $MgO/Co_{40}Fe_{40}B_{20}/Ta$ structures, Appl. Phys. Lett. **96**, 212503 (2010).

[50] W. G. Wang and C. L. Chien, Voltage-induced switching in magnetic tunnel junctions with perpendicular magnetic anisotropy, J. Phys. D: Appl. Phys. **46**, 074004 (2013).

[51] P. Khalili Amiri, J. G. Alzate, X. Q. Cai, and F. Ebrahimi, Electric-Field-Controlled magnetoelectric RAM: Progress, challenges, and scaling, Mag. IEEE Trans. **51**, 1 (2015).

[52] J. Zhu, J. A. Katine, G. E. Rowlands, Y.-J. Chen, Z. Duan, J. G. Alzate, P. Upadhyaya, J. Langer, P. K. Amiri, K. L. Wang, and I. N. Krivorotov, Voltage-Induced Ferromagnetic Resonance in Magnetic Tunnel Junctions, Phys. Rev. Lett. **108**, 197203 (2012).

[53] J. G. Alzate, P. Khalili Amiri, G. Yu, P. Upadhyaya, J. A. Katine, J. Langer, B. Ocker, I. N. Krivorotov, and K. L. Wang, Temperature dependence of the voltage-controlled perpendicular anisotropy in nanoscale MgO/CoFeB/Ta magnetic tunnel junctions, Appl. Phys. Lett. **104**, 112410 (2014).

[54] A. Vansteenkiste, J. Leliaert, M. Dvornik, M. Helsen, F. Garcia-Sanchez, and B. Van Waeyenberge, The design and verification of MuMax3, AIP Adv. **4**, 107133 (2014).

[55] M. Mohseni, D. R. Rodrigues, M. Saghafi, S. Chung, M. Ahlberg, H. F. Yazdi, Q. Wang, S. A. H. Banuazizi, P. Pirro, J. Åkerman, and M. Mohseni, Chiral excitations of magnetic droplet solitons driven by their own inertia, Phys. Rev. B **101**, 020417 (2020).

[56] P. Wills, E. Iacocca, and M. Hoefer, Deterministic drift instability and stochastic thermal perturbations of magnetic dissipative droplet solitons, Phys. Rev. B **93**, 144408 (2016).

[57] D. Xiao, Y. Liu, Y. Zhou, S. M. Mohseni, S. Chung, and J. Åkerman, Merging droplets in double nanocontact spin torque oscillators, Phys. Rev. B **93**, 094431 (2016).

[58] See Supplemental Material at http://link.aps.org/supplemental/10.1103/PhysRevApplied.14.054001 for the full movies of the simulations.

[59] D. Xiao, V. Tiberkevich, Y. H. Liu, Y. W. Liu, S. M. Mohseni, S. Chung, M. Ahlberg, A. N. Slavin, J. Åkerman, and Y. Zhou, Parametric autoexcitation of magnetic droplet soliton perimeter modes, Phys. Rev. B **95**, 024106 (2017).

[60] D. D. Sheka, C. Schuster, B. A. Ivanov, and F. G. Mertens, Dynamics of topological solitons in two-dimensional ferromagnets, Eur. Phys. J. B **50**, 393 (2006).

[61] G. Consolo, L. Lopez-Diaz, L. Torres, G. Finocchio, A. Romeo, and B. Azzerboni, Nanocontact spin-transfer oscillators based on perpendicular anisotropy in the free layer, Appl. Phys. Lett. **91**, 162506 (2007).

[62] M. Mohseni, M. Hamdi, H. F. Yazdi, S. A. H. Banuazizi, S. Chung, S. R. Sani, J. Åkerman, and M. Mohseni, Magnetic droplet soliton nucleation in oblique fields, Phys. Rev. B **97**, 184402 (2018).